Research Article | Vol. 31, No. 6 / 13 Mar 2023 / Optics Express 9515
Optics EXPRESS

Femtosecond laser upgrading the quality of bismuth films to enhance ultra-broadband photodetection

YUCAI LIN,[1,2] SHUXIA CHEN,[3] CHANG XU,[3] ZIPU FAN,[3] TINGTING ZOU,[1,2,4] DONG SUN,[3] AND JIANJUN YANG[1,2,*]

[1]GPL Photonics Laboratory, State Key Laboratory of Luminescence and Applications, Changchun Institute of Optics, Fine Mechanics and Physics, Chinese Academy of Sciences, Changchun, 130033, China
[2]Center of Materials Science and Optoelectronics Engineering, University of Chinese Academy of Sciences, Beijing, 100049, China
[3]International Center for Quantum Materials, School of Physics, Peking University, Beijing 100871, China
[4]zoutingting@ciomp.ac.cn
*jjyang@ciomp.ac.cn

Abstract: Topological insulator bismuth has attracted considerable attention for the fabrication of room-temperature, wide bandwidth, and high-performance photodetectors due to the gapless edge state and insulating bulk state properties. However, both the photoelectric conversion and carrier transportation of the bismuth films are extremely affected by the surface morphology and grain boundaries to limit optoelectronic properties further. Here, we demonstrate a strategy of femtosecond laser treatment for upgrading the quality of bismuth films. After the treatment with proper laser parameters, the measurement of average surface roughness can be reduced from $R_a = 44$ nm to 6.9 nm, especially with accompany of the evident grain boundary elimination. Consequently, the photoresponsivity of the bismuth films increases approximately 2 times within an ultra-broad spectrum range from the visible to mid-infrared. This investigation suggests that the femtosecond laser treatment can help to benefit the performance of topological insulator ultra-broadband photodetectors.

1. Introduction

A design of broadband photodetectors spanning the ultraviolet to the far-infrared and even terahertz ranges is of great interest for communications, biomedicine, remote sensing, and other fields [1–5]. However, the response spectrum of commercial photodetectors is usually limited. For example, the commonly used Si-based photodetectors only work in the visible range due to the bandgap limitation, while infrared detection materials, such as indium gallium arsenic (InGaAs), indium telluride (In_2Te_3), cadmium mercury telluride (CdHgTe), cannot be used in an ultra-broadband range from the visible to mid-infrared (MIR), and the cryogenic cooling conditions are often needed as well [6,7]. Currently, the development of room-temperature ultra-broadband photodetectors is urgently required.

Emerging topological quantum materials (TQM) such as topological insulators (TI) and topological semimetal (TSM) has recently attracted significant attention in the fundamental science because of their topological surface states protected by spin-orbit coupling effects and time-reversal symmetry. Their unique properties, including the linear dispersion relations, the ultra-high carrier mobility, the special band structure, and the tunable bandgap, make them prevailing for broadband photodetectors working in the room temperature environment [8,9]. For instance, $TaIrTe_4$, Bi_2Te_3, and other TQM have been realized to cover the broadband detection from UV to IR. However, the low damage threshold of 2D layered TQM, such as graphene, is unsuitable for high laser power detection [10]. As one of the TI materials, bismuth (Bi) has been

#482018 https://doi.org/10.1364/OE.482018
Journal © 2023 Received 30 Nov 2022; revised 3 Feb 2023; accepted 7 Feb 2023; published 28 Feb 2023

Optics EXPRESS

proven to offer the potential of a broader band response than other TQM in the room temperature environment because of its bulk bandgap around 0.2 eV with the small electron effective mass, the long carrier mean free path, and the higher damage threshold [11–18]. Therefore, Bi has been widely used in the photoelectric field, such as broadband absorbers [19], photodetectors [20–24], and Hall sensors [25,26].

The quality of Bi films, including surface morphology, crystal grain size and boundary, can directly affect the photoelectric conversion and carrier transportation, which significantly determine their optoelectronic properties. To obtain this material with high quality, both technologies of the molecular beam epitaxy (MBE) [27–29] and pulsed laser deposition (PLD) [30] have been demonstrated. However, they are usually limited by the substrate lattice matching and only work on some particular substrates to confine the industry applications. Although magnetron sputtering has been proven a low-cost, facile technique for thin film fabrication, both high surface roughness and the obvious grain boundary are usually caused during this process, unavoidably leading to carriers scattering, recombination, and low responsivity for optoelectronic applications [25,26,31,32]. In order to improve the quality of Bi film after magnetron sputtering, some polishing and annealing methods are very required for further treatment. Although heat annealing process is useful for addressing the grain orientation, the residual stress and other properties, it usually suffers from high-temperature and time-consuming procedures. More importantly, the thermal annealing process can only take place for the whole sample and is unable to perform the spatially localized treatment on materials [33–36]. However, for topological insulator materials, the modification of the topological surface state is extremely important to improve their photoelectric properties [37]. Despite providing the capability of surface modification, the conventional mechanical polishing is often plagued by issues such as poor quality, low efficiency, subsurface damage, and thermal oxidation [38,39]. Therefore, it is essential to develop a novel strategy to improve or modulate the quality of Bi films.

In fact, as an intriguing approach to having the non-contact high precision manufacture on various materials, the femtosecond (fs) laser processing can also be considered for effective surface upgrading due to its ultra-high peak power and ultra-short time duration characteristics [40–43]. Fs laser irradiation can modulate not only the surface morphology but also the physiochemistry properties of materials, leading to wide applications in the fields of optoelectronics, topological phase modulation, etc. For instance, Kong et al. reported to remove of around 20 nm-thick top layer on the perovskite with irradiation of fs laser pulses, which consequently results in a decrease of surface roughness from $R_a = 42$ nm to 22 nm to improve the performance of solar cells [44]. On the other hand, femtosecond laser is also an effective tool for enhancing the photoelectric properties of materials. Song et al. used the femtosecond laser to modulate the structure and exciton kinetics of two-dimensional halide perovskites for enhancing the light response and stability, the photocurrent is increased beyond 5 times after laser treatment [45]. Huo et al. used the localized femtosecond laser irradiation process to improve MoS_2−metal contact behavior and remove the organic contamination induced by the transfer process, significantly improving the photoresponsivity of MoS_2 photodetector, which is approximately 80 times higher than the pristine one [46].

In this paper, we propose a strategy of fs laser treatment for upgrading the quality of Bi films. For the optimal laser processing parameters, it is found that the surface roughness of the sample can reduce greatly, associated with the disappearance of grain boundaries on the interface. Moreover, an optoelectronic device is fabricated on a large surface area of the efficient femtosecond laser treatment with cylindrical focusing conditions. Owing to the decreasing surface roughness and the eliminating grain boundaries on the Bi films after the laser treatment, the measured photoresponsivity of the device can be enhanced approximately 2 times within a wavelength range from visible to infrared This provides a new solution for improving the performance of topological insulator broadband photodetectors.

Optics EXPRESS

2. Results and discussion

2.1. Femtosecond laser upgrading of Bi films

In this work, the SiO_2-based Bi thin films (~300 nm thickness) prepared via a direct current (DC) magnetron sputtering method were presented for further fs laser treatment. As shown by a schematic diagram in Fig. 1, a commercial Ti:sapphire femtosecond laser amplifier (Spitfire Ace, Spectra Physics) was employed as a light source to deliver the linearly polarized infrared (800 nm, 1 kHz, 40 fs) pulse trains. After the beam expanded it was focused by a cylindrical lens (with a focal length f = 50 mm) on the Bi films that are fixed on a high precision three-dimensional translation stage, leading to a line-shaped beam spot with a diameter of about 30 mm. A large area of surface treatment was accomplished by the sample scanning process at the speed of 1 mm/s. To be surprising, after the fs laser irradiation, both the external surface morphology and the internal grain boundaries can be simultaneously manipulated, which are respectively indicated by the left and right part pictures of Fig. 1.

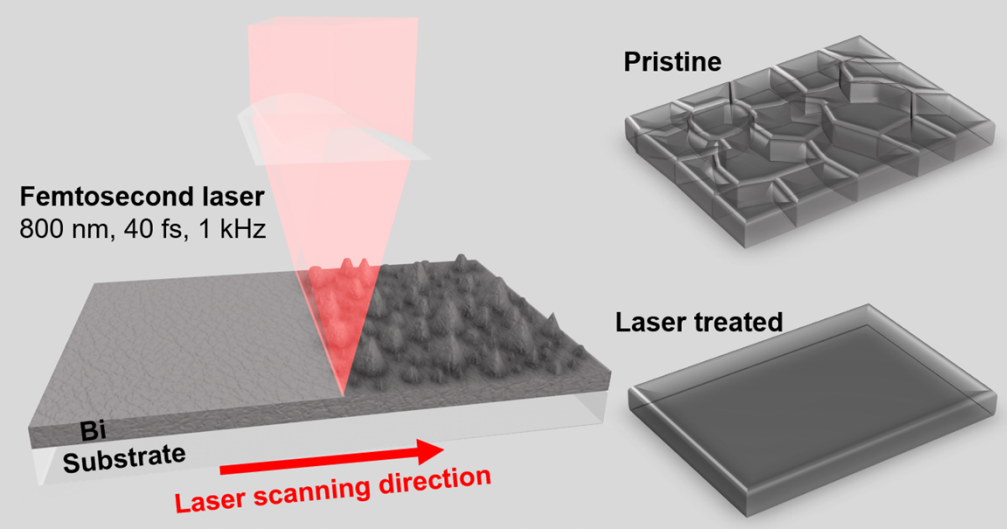

Fig. 1. Schematic diagram of the femtosecond laser treatment of Bi films.

2.2. Modulations in surface morphology and grain boundary

To better understand the effect of laser parameters on both the surface roughness and the crystal grain boundary for Bi films, we experimentally investigated the evolution of laser-treated surfaces with the incident energy fluence per pulse.

Figure 2(a)-(f) present a group of atomic force microscope (AFM) images to show variations of the surface topography for different laser fluences. With gradually increasing the laser fluence per pulse from $\boldsymbol{F} = 40$ mJ/cm^2, the observation of surface roughness tends to decrease, with the available optimal smoothness at $\boldsymbol{F} = 79$ mJ/cm^2 (Fig. 2(e)). However, when the laser fluence per pulse continued to increase, the surface roughness became higher with some nanoholes of thermal melting, as shown in Fig. 2(f). which indicates the damage to the films. In order to quantitatively characterize the evolution of surface morphology with the incident laser fluence per pulse, we respectively calculated the average surface roughness $\left(R_a = \left(\frac{1}{n}\right)\sum_{i=1}^{n}|y_i|\right)$ and the root mean square average surface roughness $\left(R_q = \sqrt{\left(\frac{1}{n}\right)\sum_{i=1}^{n}y_i^2}\right)$. of the films for different

Optics EXPRESS

laser fluences, where y is the height at a given pixel (i) in the image and n is the number of pixels [47]. As shown in Fig. 2 g, before the fs laser treatment, the obtained two average roughness of Bi films are given by $R_a = 44$ and $R_q = 64.3$ nm, respectively. Whereas for the laser fluence per pulse of around $\boldsymbol{F} = 79$ mJ/cm^2, the measured surface roughness can reduce to $R_a = 6.9$ nm and $R_q = 9.19$ nm, at least 6 times smaller than the pristine one. Furthermore, we also adopted the optical microscope to characterize the variation of surface roughness within the larger area of 70×70 μm^2, as shown in Fig. S1. The above characterizations show that the surface roughness of Bi films can be effectively adjusted by the fs laser processing.

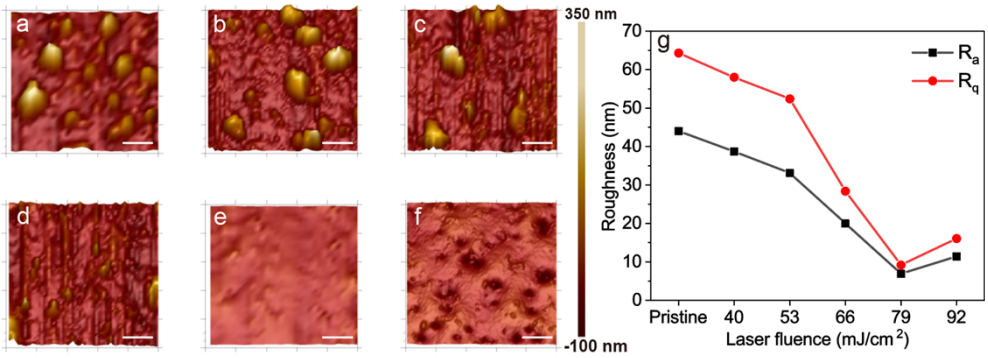

Fig. 2. Evolution of surface morphology on Bi films with the energy fluence per pulse of fs laser treatment. (a-f) AFM images, where (a) pristine film; (b) $\boldsymbol{F} = 40$ mJ/cm^2; (c) $\boldsymbol{F} = 53$ mJ/cm^2; (d) $\boldsymbol{F} = 66$ mJ/cm^2; (e) $\boldsymbol{F} = 79$ mJ/cm^2; (f) $\boldsymbol{F} = 92$ mJ/cm^2. Scale bar: 1 μm. (g) Calculated average surface roughness (R_a) and root mean square average surface roughness (R_q) as a function of the laser fluence per pulse $\boldsymbol{F}$.

In addition, the high-resolution SEM images of Bi films before and after the fs laser treatments can unveil the change of crystal grain boundaries, as shown in Fig. 3(a)-(e). It is clearly seen that the grain boundaries of the film become gradually disappear when increasing $\boldsymbol{F}$. Figures 3(a)-(b) show that the pristine film consists of many grains with a wide size distribution from tens to hundreds of nanometers, and in particular, demonstrate some big protruding particles on the surface to significantly influence the smoothness. The cross-sectional SEM image identifies that the dimension of such protruding particles is even larger than the thickness of the pristine film. In Fig. 3(c), when $\boldsymbol{F} = 53$ mJ/cm^2, the large protruding particles on the film began to disappear with the increase of grain sizes and surface uniformity due to the grain boundary elimination. When the laser fluence per pulse increases to $\boldsymbol{F} = 79$ mJ/cm^2, as shown in Fig. 3(e), the grain boundaries turn to almost disappear completely. In this case, the cross-sectional SEM image of Bi films is shown in Fig. 3(f), where the big protruding particles disappeared in all to make the surface optimally smooth. To further clarify the surface change, the higher magnification images of cross-sectional SEM are obtained in Fig. 3 g, h. It is clear that the laser-induced modification mainly occurs within a location range of approximately 80 nm from the top surface to eliminate the grain boundaries, which makes the surface layer more continuous. Moreover, the measured thickness of the pristine Bi films without protruding large grains is about 200 nm, and it was found to grow to 240 nm after the laser treatment. This is presumably due to the laser energy fluence per pulse $\boldsymbol{F} = 79$ mJ/cm^2 exceeding the ablation threshold of the material [48]. At this point, the incident femtosecond laser can melt and spall the big protruding grains on the top surface and finally develop into a boundary-free state with an increased thickness. For the topological insulators, because the carrier transportation mainly originates from the non-scattering surface state, the surface modification process can promote the electrical performance.

Optics EXPRESS

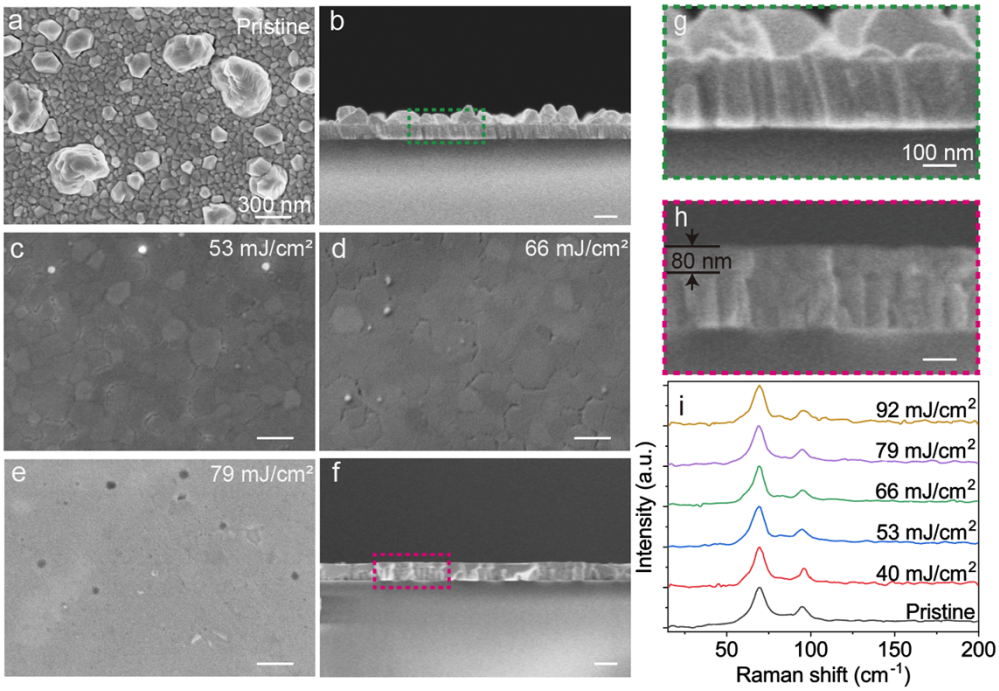

Fig. 3. SEM and Raman analyses of Bi films. (a)-(b) Top-view and cross-section SEM images of the pristine film; (c)-(e) SEM images of the laser treated Bi films with variable laser fluences of $\boldsymbol{F} = 53$ mJ/cm^2, $\boldsymbol{F} = 66$ mJ/cm^2, $\boldsymbol{F} = 79$ mJ/cm^2. (f) Cross-section SEM images at $\boldsymbol{F} = 79$ mJ/cm^2, scale bar: 300 nm. The high magnification of cross-sectional SEM images for (g) the pristine and (h) the laser treated films with $\boldsymbol{F} = 79$ mJ/cm^2, scale bar: 100 nm. (i) Measured Raman spectroscopy of the pristine and the laser treated Bi films with different laser fluences.

The change of elemental compositions is also vital for understanding the optoelectrical performances of the Bi films when considering the fs laser treatment in the air environment. Here, we evaluated the composition change for the laser-exposed surfaces by Raman spectroscopy. As shown in Fig. 3(i), the obtained Raman spectrum for the pristine Bi films contains the typical scattering peaks of the in-plane E_g and out-of-plane A_{1g} vibration modes at 69 cm^{-1} and 95 cm^{-1}, respectively; while after the laser treatment with different energy fluences, the Bi films exhibit no additional peaks related to the oxidation, which is attributed to the fast change of temperature than the chemical oxidation during the fs laser treatment [49]. Moreover, the grazing incidence X-ray diffraction (GIXRD) measurements were also carried out to show the same peak profiles as the standard XRD, which not only confirms that no oxidation is happening on the Bi film surface, but also indicates that the crystal orientation of Bi remains almost unchanged during laser treatment (Fig. S2).

More interestingly, to investigate the stable properties of the laser-treated Bi sample working within air environment, we applied intense light radiation (473 nm, 1.5×10^3 W/cm^2, 5 s) on it, and the subsequent photoluminescence (PL) characterization only showed a weak peak of the material oxidation (Fig. S3). Such good withstanding behaviors lay a solid foundation for the high-performance self-powered Bi photodetectors.

Optics EXPRESS

2.3. Optoelectronic performances of the reformed Bi films

The optoelectronic performance of the laser-treated Bi films was evaluated with broadband laser excitation. The preparation of optoelectronic devices was based on the sample treated with the laser fluence per pulse of $\boldsymbol{F} = 79$ mJ/cm^2, $v = 1$ mm/s, because it has the minimum surface roughness and the eliminated grain boundaries. By adopting the beam expansion and the cylindrical focusing conditions, we accomplished a large area (10×10 mm^2) of the film surface in one step without splicing. The laser processing efficiency can reach about $\eta = 18$ cm^2/min. The optical image with an inset picture shown in Fig. 4(a) compares the morphologies of two parts of the sample surface before (left) and after (right) the laser treatments. Clearly, even with the centimeter-scale laser processing, the surface roughness of the sample can be greatly reduced by the disappearance of large protruding particles. We also employed an atomic force microscope (AFM) to characterize the morphology change of the film surface in three dimensions (3D), as shown in Fig. 4(b), c, where the protruding particles on the Bi film surface are effectively removed to make the surface morphology significantly smooth. By comparing the measured AFM data before and after the laser treatments, we can find their average height difference of about $\Delta h = 200$ nm, associated with the maximum value of about 300 nm.

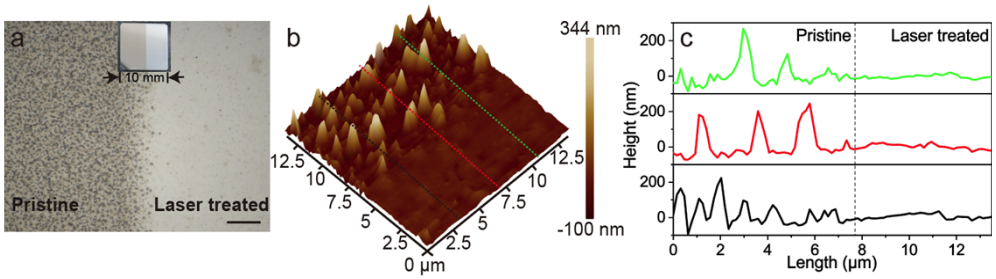

Fig. 4. Comparison of the surface roughness before and after laser treatment ($\boldsymbol{F} = 79$ mJ/cm^2) of Bi film. (a) Optical image of the pristine (left) and treated (right) Bi film, scale bar: 10 μm. Inset: 10×10 mm^2 Bi film on the SiO_2 substrate. (b) AFM image of the boundary of the pristine (upper left) and laser treated (lower right) Bi film. (c) Comparison of surface profiles before and after the laser treatment corresponding to the lines in (b).

Figure 5(a) shows a schematic diagram of the fabricated Ag-Bi-Ag devices on the SiO_2 substrate, where two Ag electrodes are connected for the photocurrent (PC) measurement. The available PC response originated from two parts: the interface of Bi-Ag junctions and the inner area of Bi films away from the metal electrodes. Because of the predominant photothermoelectric effect, the photocurrent signals are mainly collected from the interface of the junctions in our work.

Taking advantage of the topologically protected gapless surface band structure and the photothermoelectric property, the PC responses of the Bi device are able to cover a broad wavelength range. Here, three typical wavelengths from the visible to MIR (532 nm, 4 μm, and 10.6 μm) were selected to compare the photoresponse of the pristine and the laser treated Bi film photodetectors. Figure 5(b)-(d) illustrate the short-circuit PC responses at different excitation wavelengths. The employed powers for three wavelengths are 5 mW (532 nm), 1.05 mW (4 μm), and 0.85 mW (10.6 μm), respectively. It is interestingly found that after the laser treatment all the responsivities for the three wavelengths can increase by nearly 100%. In addition, both the photoresponse curves with the variation of excitation energy and their stability measurements were explored in the experiment (Fig. S4). We also performed the Vis-NIR and MIR absorption spectra for both the pristine and laser-treated Bi films, as shown in Fig. S5. For the case of laser-treated Bi films, even though the optical absorption was decreased by about 40%, it was

Optics EXPRESS

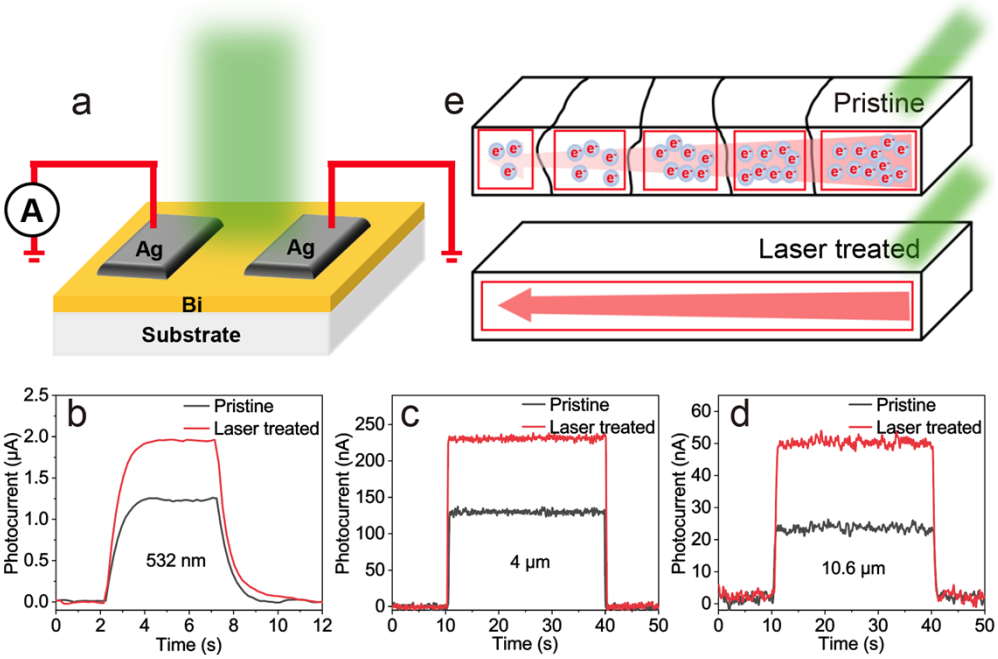

Fig. 5. Bi film broadband photodetector. (a) Schematics of the device layout. (b-d) Broadband photoresponse of pristine and laser-treated Bi film photodetector for different excitation wavelengths: (b) 532 nm, (c) 4 μm, (d) 10.6 μm at room temperature. (e) Schematic diagram of the carrier transportation enhancement mechanism.

unexpectedly found that the measurement of its responsivity can still increase, which indicates a more than 160% increment in the actual internal responsivity. It further proves the improved efficiency of photoelectric conversion and photogenerated carrier transportation.

The physical mechanisms of the carrier transportation enhancement for two surface parts of the pristine and the laser-treated Bi films are illustrated in Fig. 5(e). As analyzed with SEM images in Fig. 3 g, h, the grain boundaries in the films disappeared after the laser treatment, which can help the photogenerated carriers easily transport from the excitation area to other parts [50]. Especially for the topological insulator material before the laser treatment (Fig. 5(e) upper), the topological protect surface state tends to make the carriers transport circularly within the grains, so that the efficiency of carrier transportation among different grains becomes very low to make the carriers decay fast. In comparison, the laser-treated Bi film (Fig. 5(e) bottom) would like to lower the recombination rate of photogenerated charge carriers. In other words, the available slower recombination rate implies the better separation between the photogenerated electrons and holes due to the higher continuity of the sample surface, which significantly suppresses the recombination of photo-generated charge carriers. This result is consistent with the measured higher photoresponse performance of the laser-treated Bi films within the broadband range.

2.4. Discussion

The flexible femtosecond laser treatment enables the precise modulation of surface roughness and grain boundary in Bi films. Unlike the traditional mechanical polishing and annealing methods, the laser upgrading technique offers a combined solution for spatially localized processing and improved surface quality. In fact, one of the challenges for topological insulator thin films is that the bulk conductivity mixes bulk and surface transport characteristics [37]. Here, different from

Optics EXPRESS

many other efforts focusing on reducing the bulk carrier contribution, we provide a new path to manipulate the surface states in thin-film devices, increase the surface's continuity and carrier transportation ability, and emphasize the contributions of the surface state. This will increase the carrier transportation and decrease the scattering loss on the surface of topological insulator, thus improving the subsequent photoelectricity. Therefore, this method can also be employed for other topological insulator films to obtain a smooth and grain boundary-free surface, thus enhancing photoelectric properties.

This work focuses on a new strategy for improving the quality of topological insulator films. As a matter of fact, with the help of optimizing laser parameters and other assisted modalities, the photoelectric conversion efficiency can be further improved easily. For example, in a combination of multiple laser scanning, the surface smoothness can be effectively optimized, or the laser treatment of the sample in the vacuum environment can reduce particles sputtering on the surface. Furthermore, the future design of special patterns with a fs-laser-induced-periodic-surface-structures (LIPSS) method is also promising to enhance the optical absorption of Bi films. All these approaches have opportunities to improve the performance of photoelectric devices.

3. Conclusion

In summary, we have demonstrated that the femtosecond laser processing can be employed as an effective method to reform the Bi films, including two aspects of surface roughness and grain boundary. With tunable laser parameters, not only the surface roughness of the films can be continuously changed, but also the grain boundaries are eliminated simultaneously, thus leading to the significant improvement of carrier transportation. Compared with the pristine sample, the laser-treated Bi films have exhibited a two-fold increase of photoresponsivity for a broadband range from the visible to MIR even at room temperature. In general, this method can be further used for improving the quality of other topological insulators, which certainly promotes the application of topological insulator materials in the field of ultra-broadband photoelectric detection.

4. Experimental section

Bi films preparation: 300 nm thick Bi thin film over the SiO_2 substrate was fabricated via Direct current (DC) magnetron sputtering. The base pressure in the sputter deposition chamber is 5×10^{-4} Pa, and the high-purity Bi (99.99%) targets are sputtered in a pure Ar atmosphere. During the sputtering process, the deposition parameters were set as follows: deposition rate: 2.5 Å/s; pressure: 1 Pa. The deposition of Bi films was carried out at room temperature.

Fs laser processing parameters: A commercial Ti:sapphire femtosecond laser amplifier (Spitfire Ace, Spectra Physics) was employed as a light source to deliver the linearly polarized infrared ($\lambda = 800$ nm) pulse trains with the repetition rate of 1 kHz, leading to a large time interval of 1 ms between the two adjacent pulses. The pulse duration of the laser is 40 fs. The energy of the laser pulses was finely adjusted by a combination of a half-wave plate with a Glan-Taylor prism. Afterward, to provide a large spot with a less radical change of the intensity, the laser beam was expanded to 30 mm diameter by a pair of convex and concave lenses and then focused by a cylindrical lens (with a focal length $f = 50$ mm) into a line-shaped beam spot. The measured spatial distribution of the focused laser spot using a CCD camera is 30 mm × 5 μm in the experiment. Under the fixed irradiation of fs lasers, the Bi film sample was mounted on a computer-controlled X-Y-Z stage (XMS-100, Newport) to translate at a velocity of $v = 1$ mm/s. The efficient number of laser pulses per site is estimated $N_{eff} = 5$. For the optimized laser fluence per pulse 79 mJ/cm^2, the integrated fluence is 395 mJ/cm^2.

Device fabrication and photoresponse measurements: The Bi film was covered by a pair of Ag (80 nm) electrodes using thermal evaporation process with deposition rates of 0.08 nm/s. For wavelength-dependent measurements, in visible regime, a CW 532 nm laser is used for

Optics EXPRESS

excitation, and the short-circuit PC signal was measured in ambient conditions with a Keithley 4200A semiconductor parametric analyzer (Tektronix) and a C-100 probe station (TPSi). For MIR regime, two CW quantum cascade laser sources emitting at 4 and 10.6 μm are used for measurement. The MIR beams were focused by a 40× reflection objective lens. The laser beam was modulated with a mechanical chopper, and the short-circuit PC signal was detected with a current pre-amplifier and a lock-in amplifier.

Characterization: Optical images were obtained by KEYENCE VK-X200 3D laser scanning microscope. AFM was obtained by BRUKER MULTIMODE 8. SEM characterizations were performed with Hitachi S-4800. The GIXRD was characterized by BRUKER D8 Advance. Raman and PL measurements (HORIBA Scientific Raman Spectrometer) were carried out under the wavelength of 532 nm and 473 nm laser, respectively, with a 50× objective lens. The absorption spectrum is obtained by Cary 5000 spectrophotometer (Agilent) for Vis-NIR and Cary 630 (Agilent) for MIR.

Funding. Strategic Priority Research Program of Chinese Academy of Sciences (XDA22010302); China Postdoctoral Science Foundation (2022M713068, 2022T150633); Jilin Provincial Science & Technology Development Project (20200201086JC).

Disclosures. The authors declare that there are no conflicts of interest related to this article.

Data availability. Data underlying the results presented in this paper are not publicly available at this time but may be obtained from the authors upon reasonable request.

Supplemental document. See Supplement 1 for supporting content.

References

1. P. Bai, X. Li, N. Yang, W. Chu, X. Bai, S. Huang, Y. Zhang, W. Shen, Z. Fu, D. Shao, Z. Tan, H. Li, J. Cao, L. Li, E. H. Linfield, Y. Xie, and Z. Zhao, "Broadband and photovoltaic THz/IR response in the GaAs-based ratchet photodetector," Sci. Adv. **8**(21), eabn2031 (2022).
2. C. Li, H. Wang, F. Wang, T. Li, M. Xu, H. Wang, Z. Wang, X. Zhan, W. Hu, and L. Shen, "Ultrafast and broadband photodetectors based on a perovskite/organic bulk heterojunction for large-dynamic-range imaging," Light: Sci. Appl. **9**(1), 31 (2020).
3. J. Lai, Y. Liu, J. Ma, X. Zhuo, Y. Peng, W. Lu, Z. Liu, J. Chen, and D. Sun, "Broadband Anisotropic Photoresponse of the "Hydrogen Atom" Version Type-II Weyl Semimetal Candidate TaIrTe4," ACS Nano **12**(4), 4055–4061 (2018).
4. L. Zhang, I. Song, J. Ahn, M. Han, M. Linares, M. Surin, H.-J. Zhang, J. H. Oh, and J. Lin, "π-Extended perylene diimide double-heterohelicenes as ambipolar organic semiconductors for broadband circularly polarized light detection," Nat. Commun. **12**(1), 142 (2021).
5. X. Lu, P. Jiang, and X. Bao, "Phonon-enhanced photothermoelectric effect in SrTiO3 ultra-broadband photodetector," Nat. Commun. **10**(1), 138 (2019).
6. Y. Chen, Z. Xie, J. Huang, Z. Deng, and B. Chen, "High-speed uni-traveling carrier photodiode for 2μm wavelength application," Optica **6**(7), 884–889 (2019).
7. B. Sun, A. M. Najarian, and L. K. Sagar, *et al.*, "Fast Near-Infrared Photodetection Using III-V Colloidal Quantum Dots," Adv. Mater. **34**, e2203039 (2022).
8. X. Zhang, J. Wang, and S.-C. Zhang, "Topological insulators for high-performance terahertz to infrared applications," Phys. Rev. B **82**(24), 245107 (2010).
9. L. Wang, L. Han, W. Guo, L. Zhang, C. Yao, Z. Chen, Y. Chen, C. Guo, K. Zhang, C. N. Kuo, C. S. Lue, A. Politano, H. Xing, M. Jiang, X. Yu, X. Chen, and W. Lu, "Hybrid Dirac semimetal-based photodetector with efficient low-energy photon harvesting," Light: Sci. Appl. **11**(1), 53 (2022).
10. C. Bao, P. Tang, D. Sun, and S. Zhou, "Light-induced emergent phenomena in 2D materials and topological materials," Nat. Rev. Phys. **4**(1), 33–48 (2022).
11. C. H. Hsu, X. Zhou, T. R. Chang, Q. Ma, N. Gedik, A. Bansil, S. Y. Xu, H. Lin, and L. Fu, "Topology on a new facet of bismuth," Proc. Natl. Acad. Sci. **116**(27), 13255–13259 (2019).
12. F. Schindler, Z. Wang, M. G. Vergniory, A. M. Cook, A. Murani, S. Sengupta, A. Y. Kasumov, R. Deblock, S. Jeon, I. Drozdov, H. Bouchiat, S. Guéron, A. Yazdani, B. A. Bernevig, and T. Neupert, "Higher-order topology in bismuth," Nat. Phys. **14**(9), 918–924 (2018).
13. L. Aggarwal, P. Zhu, T. L. Hughes, and V. Madhavan, "Evidence for higher order topology in Bi and $Bi_{0.92}Sb_{0.08}$," Nat. Commun. **12**(1), 4420 (2021).
14. A. K. Nayak, J. Reiner, R. Queiroz, H. Fu, C. Shekhar, B. Yan, C. Felser, N. Avraham, and H. Beidenkopf, "Resolving the topological classification of bismuth with topological defects," Sci. Adv. **5**(11), eaax6996 (2019).
15. W. Ning, F. Kong, C. Xi, D. Graf, H. Du, Y. Han, J. Yang, K. Yang, M. Tian, and Y. Zhang, "Evidence of Topological Two-Dimensional Metallic Surface States in Thin Bismuth Nanoribbons," ACS Nano **8**(7), 7506–7512 (2014).

Optics EXPRESS

16. W. Kang, F. Spathelf, B. Fauque, Y. Fuseya, and K. Behnia, "Boundary conductance in macroscopic bismuth crystals," Nat. Commun. **13**(1), 189 (2022).
17. S. Xiao, D. Wei, and X. Jin, "Bi(111) Thin Film with Insulating Interior but Metallic Surfaces," Phys. Rev. Lett. **109**(16), 166805 (2012).
18. Y. Park, Y. Hirose, S. Nakao, T. Fukumura, J. Xu, and T. Hasegawa, "Quantum confinement effect in Bi anti-dot thin films with tailored pore wall widths and thicknesses," Appl. Phys. Lett. **104**(2), 023106 (2014).
19. M. C. Soydan, A. Ghobadi, D. U. Yildirim, E. Duman, A. Bek, V. B. Erturk, and E. Ozbay, "Lithography-Free Random Bismuth Nanostructures for Full Solar Spectrum Harvesting and Mid-Infrared Sensing," Adv. Opt. Mater. **8**(4), 1901203 (2020).
20. Q. Zhou, D. Lu, H. Tang, S. Luo, Z. Li, H. Li, X. Qi, and J. Zhong, "Self-Powered Ultra-Broadband and Flexible Photodetectors Based on the Bismuth Films by Vapor Deposition," ACS Appl. Electron. Mater. **2**(5), 1254–1262 (2020).
21. J. D. Yao, J. M. Shao, and G. W. Yang, "Ultra-broadband and high-responsive photodetectors based on bismuth film at room temperature," Sci. Rep. **5**(1), 12320 (2015).
22. T. E. Huber, S. D. Johnson, J. H. Belk, J. H. Hunt, and K. Shirvani, "Charge Transfer and Photocurrent in Interfacial Junctions between Bismuth and Graphene," Phys. Rev. Appl. **10**(4), 044020 (2018).
23. Z. Dang, W. Wang, J. Chen, E. S. Walker, S. R. Bank, D. Akinwande, Z. Ni, and L. Tao, "Vis-NIR photodetector with microsecond response enabled by 2D bismuth/Si(111) heterojunction," 2D Mater. **8**(3), 035002 (2021).
24. J. Yao, Z. Zheng, J. Shao, and G. Yang, "Promoting Photosensitivity and Detectivity of the Bi/Si Heterojunction Photodetector by Inserting a WS2 Layer," ACS Appl. Mater. Interfaces **7**(48), 26701–26708 (2015).
25. M. Melzer, J. I. Mönch, D. Makarov, Y. Zabila, G. S. Cañón Bermúdez, D. Karnaushenko, S. Baunack, F. Bahr, C. Yan, M. Kaltenbrunner, and O. G. Schmidt, "Wearable Magnetic Field Sensors for Flexible Electronics," Adv. Mater. **27**(7), 1274–1280 (2015).
26. A. Pilidi, A. Tzanis, T. Helm, M. Arfanis, P. Falaras, and T. Speliotis, "Nanometer-Thick Bismuth Nanocrystal Films for Sensoric Applications," ACS Appl. Nano Mater. **3**(10), 9669–9678 (2020).
27. G. Sciaini, M. Harb, S. G. Kruglik, T. Payer, C. T. Hebeisen, F.-J. M. Z. Heringdorf, M. Yamaguchi, M. H.-V. Hoegen, R. Ernstorfer, and R. J. D. Miller, "Electronic acceleration of atomic motions and disordering in bismuth," Nature **458**(7234), 56–59 (2009).
28. D. M. Fritz, D. A. Reis, and B. Adams, *et al.*, "Ultrafast bond softening in bismuth: mapping a solid's interatomic potential with X-rays," Science **315**(5812), 633–636 (2007).
29. E. S. Walker, S. R. Na, D. Jung, S. D. March, J.-S. Kim, T. Trivedi, W. Li, L. Tao, M. L. Lee, K. M. Liechti, D. Akinwande, and S. R. Bank, "Large-Area Dry Transfer of Single-Crystalline Epitaxial Bismuth Thin Films," Nano Lett. **16**(11), 6931–6938 (2016).
30. Z. Yang, Z. Wu, Y. Lyu, and J. Hao, "Centimeter-scale growth of two-dimensional layered high-mobility bismuth films by pulsed laser deposition," InfoMat **1**(1), 98–107 (2019).
31. W. Huang, J. Zhu, M. Wang, L. Hu, Y. Tang, Y. Shu, Z. Xie, and H. Zhang, "Emerging Mono-Elemental Bismuth Nanostructures: Controlled Synthesis and Their Versatile Applications," Adv. Funct. Mater. **31**(10), 2007584 (2021).
32. A. Reyes-Contreras, M. Camacho-Lopez, S. Camacho-Lopez, O. Olea-Mejia, A. Esparza-Garcia, J. G. Banuelos-Muneton, and M. A. Camacho-Lopez, "Laser-induced periodic surface structures on bismuth thin films with ns laser pulses below ablation threshold," Opt. Mater. Express **7**(6), 1777–1786 (2017).
33. Y. Cao, H. Yang, Y. Zhao, Y. Zhang, T. Ren, B. Jin, J. He, and J.-L. Sun, "Fully Suspended Reduced Graphene Oxide Photodetector with Annealing Temperature-Dependent Broad Spectral Binary Photoresponses," ACS Photonics **4**(11), 2797–2806 (2017).
34. J. Park, J. W. Choi, W. Kim, R. Lee, H. C. Woo, J. Shin, H. Kim, Y. J. Son, J. Y. Jo, H. Lee, S. Kwon, C.-L. Lee, and G. Y. Jung, "Improvement of perovskite crystallinity by omnidirectional heat transfer via radiative thermal annealing," RSC Adv. **9**(26), 14868–14875 (2019).
35. T. Jeon, H. M. Jin, S. H. Lee, J. M. Lee, H. I. Park, M. K. Kim, K. J. Lee, B. Shin, and S. O. Kim, "Laser Crystallization of Organic-Inorganic Hybrid Perovskite Solar Cells," ACS Nano **10**(8), 7907–7914 (2016).
36. C. Song, L. Tong, F. Liu, L. Ye, and G. J. Cheng, "Addressing the Reliability and Electron Transport Kinetics in Halide Perovskite Film via Pulsed Laser Engineering," Adv. Funct. Mater. **30**, 1906781 (2019).
37. J. J. Cha and Y. Cui, "The surface surfaces," Nat. Nanotechnol. **7**(2), 85–86 (2012).
38. Y. Gu, W. Zhu, J. Lin, M. Lu, and M. Kang, "Subsurface Damage in Polishing Process of Silicon Carbide Ceramic," Materials **11**(4), 506 (2018).
39. R. Koseva, I. Mönch, D. Meier, J. Schumann, K. F. Arndt, L. Schultz, B. Zhao, and O. G. Schmidt, "Evolution of hillocks in Bi thin films and their removal upon nanoscale mechanical polishing," Thin Solid Films **520**(17), 5589–5592 (2012).
40. Y. Zhang, Q. Jiang, M. Long, R. Han, K. Cao, S. Zhang, D. Feng, T. Jia, Z. Sun, J. Qiu, and H. Xu, "Femtosecond laser-induced periodic structures: mechanisms, techniques, and applications," Opto-Electron. Sci. **1**(6), 220005 (2022).
41. Z. Deng, Q. Yang, F. Chen, X. Meng, H. Bian, J. Yong, C. Shan, and X. Hou, "Fabrication of large-area concave microlens array on silicon by femtosecond laser micromachining," Opt. Lett. **40**(9), 1928–1931 (2015).

Optics EXPRESS

42. T. Zou, B. Zhao, W. Xin, Y. Wang, B. Wang, X. Zheng, H. Xie, Z. Zhang, J. Yang, and C. L. Guo, "High-speed femtosecond laser plasmonic lithography and reduction of graphene oxide for anisotropic photoresponse," Light: Sci. Appl. **9**(1), 69 (2020).
43. H. Liu, W. Lin, and M. Hong, "Hybrid laser precision engineering of transparent hard materials: challenges, solutions and applications," Light: Sci. Appl. **10**(1), 162 (2021).
44. W. Kong, C. Zhao, J. Xing, Y. Zou, T. Huang, F. Li, J. Yang, W. Yu, and C. Guo, "Enhancing Perovskite Solar Cell Performance through Femtosecond Laser Polishing," Sol. RRL **4**(7), 2000189 (2020).
45. C. Song, H. Yang, F. Liu, and G. J. Cheng, "Ultrafast femtosecond pressure modulation of structure and exciton kinetics in 2D halide perovskites for enhanced light response and stability," Nat. Commun. **12**(1), 4879 (2021).
46. J. Huo, Y. Xiao, T. Sun, G. Zou, D. Shen, B. Feng, L. Lin, W. Wang, G. Zhao, and L. Liu, "Femtosecond Laser Irradiation-Mediated MoS_2–Metal Contact Engineering for High-Performance Field-Effect Transistors and Photodetectors," ACS Appl. Mater. Interfaces **13**(45), 54246–54257 (2021).
47. Nanosurf, "Topography and surface roughness measurements," (2022), https://www.nanosurf.com/en/support/afm-modes-overview/topography-and-surface-roughness-measurements.
48. R. Santillan, A. Wong, P. Segovia, M. Camacho-Lopez, and S. Camacho-Lopez, "Femtosecond laser-induced periodic surface structures formation on bismuth thin films upon irradiation in ambient air," Opt. Mater. Express **10**(2), 674–681 (2020).
49. D. Bäuerle, *Laser Processing and Chemistry* (2011).
50. L. Zhao, P. Tang, D. Luo, M. I. Dar, F. T. Eickemeyer, N. Arora, Q. Hu, J. Luo, Y. Liu, S. M. Zakeeruddin, A. Hagfeldt, J. Arbiol, W. Huang, Q. Gong, T. P. Russell, R. H. Friend, M. Gratzel, and R. Zhu, "Enabling full-scale grain boundary mitigation in polycrystalline perovskite solids," Sci. Adv. **8**(35), eabo3733 (2022).